Decomposition mechanism of Anisole on Pt(111). Combining single crystal experiments and first principle calculations.

Romain Réocreux,[‡] Cherif A. Ould Hamou,[†,§] Carine Michel,[‡] Javier B. Giorgi,[†,||,*] Philippe Sautet[‡,&,*]

[‡] Univ Lyon, Ens de Lyon, CNRS UMR 5182, Université Claude Bernard Lyon 1, Laboratoire de Chimie, F-69342, Lyon, France

[†] Centre for Catalysis Research and Innovation, [§] Department of Physics, [||] Department of Chemistry and Biomolecular Sciences, University of Ottawa, 10 Marie Curie Pvt., Ottawa, Ontario, Canada. K1N 6N5.

[&] Department of Chemical and Biomolecular engineering, University of California, Los Angeles, Los Angeles, CA 90095, United States

Abstract

To valorize lignin as a renewable source of aromatics, it is necessary to develop selective heterogeneous catalysts for the hydrodeoxygenation reaction of aromatic oxygenates such as anisole. Most of the metal supported catalysts tested so far exhibit a high conversion but a low selectivity towards valuable aromatic hydrocarbons, yielding mainly phenolic compounds. To gain insights into that catalytic system, we performed surface science experiments (X-ray Photoelectron Spectroscopy and Temperature Programmed Desorption) under Ultra-High Vacuum conditions (UHV). Dosing anisole on Pt(111) surprisingly gave benzene, carbon monoxide and hydrogen as the main desorbing products of decomposition. With the help of Density Functional Theory (DFT) we successfully explain the unexpected selectivity. In the present work we show in particular that phenoxy PhO stands as a key intermediate. Although the UHV conditions do not allow the hydrogenation of phenoxy into phenol, *i.e.* the catalytic product, they reveal the key role of both hydrogen and carbonaceous species. Under UHV conditions, anisole gets extensively dehydrogenated: it results in the formation of carbonaceous fragments, which can actually perform the deoxygenation of phenoxy into benzene, but also, more importantly, coke. This detailed study opens the door to a rational design of hydrodeoxygenation catalysts based on supported metals.

Keywords: Lignin, Pt(111), anisole decomposition mechanism, phenol, benzene, DFT, TPD, XPS

Introduction

Within the context of biomass conversion, lignin has received intense research for about a decade concerning its extraction and decomposition into upgradable aromatic fragments.[1–3] Lignin is indeed nature's most abundant aromatic polymer (10% to 30% of biomass) and therefore represents an extraordinary sustainable source of high valuable aromatic compounds, which are currently produced from oil fractions. Among those target molecules, the so-called BTX platform (benzene, toluene, and xylene) is of great interest. Their production however requires the deoxygenation of the aromatic monomers and oligomers obtained from preliminary lignin depolymerization. Decreasing the oxygen content of such recalcitrant phenolic compounds still remains a very difficult task. The required reduction of the oxygen containing functional groups (ethers, phenols, etc) indeed competes with the undesired reduction of the aromatic moieties into cyclic, or worse, linear alkanes.

Albeit quite challenging, many heterogeneous catalysts have been designed to reduce the amount of oxygenated functional groups using moderate to large pressures of hydrogen. This so-called hydrodeoxygenation (HDO) reaction can be catalyzed using molybdenum sulfide catalysts promoted with cobalt or nickel (CoMoS or NiMoS).[4–7] To maintain their catalytic activity, *extra* sulfur-containing species must however be added to the system, leading to an undesired increase of the sulfur content in the products.[8] The HDO of lignin fragments has also been attempted on noble metals. Ru and Pd show higher conversion for HDO than CoMoS and NiMoS.[9] Pt shows even higher conversions but the products are not as deoxygenated as with the other noble metals. This singularity of Pt has been investigated a lot using anisole and guaiacol as model compounds. Under HDO conditions they mainly undergo demethylation or transalkylation reactions, leading to different phenolic compounds.[10–12] In spite of the very reducing environment, only very small amounts of BTX – resulting from demethoxylation – have been detected. Even if reaction networks have been proposed,[10,13,14] the full mechanism remains difficult to elucidate experimentally since both the conditions and the support can have effects on the selectivity.[15,16]

To gain insights into the reactivity of aromatic oxygenates on noble metal surfaces, many DFT studies have been performed and published.[13,17–24] Honkela *et al.* showed in particular that the dissociation of phenol into phenoxy was endothermic on Pt(111) and exothermic on Rh(111) and suggested that it may explain the higher propensity of Rh to deoxygenate aromatics.[19] Vlachos *and co-workers* recently proposed the first DFT-elucidated mechanism of guaiacol decomposition.[20] Based on electronic energies, they showed that

guaiacol could indeed be demethylated to catechol but was recalcitrant to further deoxygenation. Heyden *and co-workers* enhanced this model taking entropy and pressure effects into account and confirmed Vlachos's work.[25] However it is very difficult to get experimental evidence that support the proposed mechanism since many parameters remain quite challenging to model (e.g. support effects, state of surfaces, …).

Fortunately, single crystal experiments can help investigating the intrinsic reactivity of the metal catalyst by isolating the different parameters like in particular the environment and the shape of the catalyst. Using TPD experiments, the reactivity of simpler aromatics has already been reported in the literature and has shown different preferences in C-H, C-O and C-C bond cleavages. Phenol has been extensively studied on various metals. On Rh(111)[26] it decomposes into phenoxy via O-H bond cleavage at temperatures below 300 K, while C-H bond cleavage is observed at 350 K and above. Observable products of desorption are CO and H_2. On Mo(110)[27] phenoxy is also formed below 300 K but it decomposes into H_2, surface oxygen and hydrocarbon fragments. All C-O bond cleavages occur by 450 K (no molecular desorption of CO is observed). On Pt(111), the O-H bond cleavage occurs even earlier, below 200 K. Above 0.7 monolayer (ML) coverage phenoxy is subject to a competitive reaction pathway, it either generates benzene and surface oxygen, or it decomposes into CO, H_2 and carbonaceous species. Below 0.5 ML coverage, no CH-containing adsorbates can be observed on the surface: C-C and C-H bond cleavages are more favorable than the C-O bond cleavage. This leads to hydrogen and carbon monoxide as the main desorbing products.[28]

The only fundamental investigation of anisole decomposition on platinum was carried out by King *and co-workers*. They studied the adsorption of anisole on Pt(100)-hex by reflection adsorption infrared spectroscopy (RAIRS) and temperature programmed desorption (TPD).[29] King's group has found that the multilayer of adsorbed anisole molecularly desorbs at 175 K. The monolayer decomposes on the surface by the cleavage of the O-Me bond around 250 K to form phenoxy and methyl. Above 350 K the phenoxy species decomposes into CO, O, and H_2. The methyl group undergoes either hydrogenation to form methane that desorbs at 325 K or dehydrogenation to form surface carbon. No formation of benzene or phenol was reported.

In this manuscript, we provide a detailed description of the interaction and decomposition pathways of anisole on a Pt(111) surface. The fundamental approach involves the combination of detailed DFT calculations with experimental techniques focusing on the monolayer and submonolayer regimes of anisole on the surface. Experimental results will be presented for X-ray photoelectron spectroscopy (XPS) and temperature programmed

desorption (TPD). In combination with a kinetic analysis of the reaction energy profiles obtained from DFT, we propose a mechanism to understand the selectivity of benzene over phenol in the desorption products. Finally, we will discuss how we can rationalize the reverse selectivity observed under HDO reaction conditions.

Experimental

The 8 mm diameter and 0.5 mm thick Platinum single crystal sample with purity of 99.999% was purchased from Princeton scientific. Experiments were carried out in a multi-technique UHV chamber (Specs GmbH) with a base pressure of 4 x 10^{-10} mbar. The Pt (111) crystal surface was cleaned by repetitive cycles of 15 min of sputtering (1.5 keV, 1 x 10^{-5} mbar Ar^{+}) at 600K, followed by annealing to 1100 K for 2 minutes. The sample cleanness was confirmed by LEED and XPS. The sample was cooled via a liquid nitrogen reservoir and heated by electron bombardment as needed. The temperature was measured by a chromel-alumel (K-type) thermocouple in contact with the back of the sample.

Anisole (+99% purity, Sigma Aldrich) was introduced to the UHV chamber through a leak valve that was connected to a gas manifold with an anisole reservoir. The reservoir was heated to 350 K to increase the vapor pressure and ensure the purity of the deposition. The gas manifold was heated accordingly to prevent condensation and allow a constant, stable flux of anisole gas into the chamber. Exposure of anisole to the surface was typically performed at $1x10^{-8}$ torr pressure and the dosage measured in Langmuirs (1L = $1x10^{-6}$ torr.s).

All doses were subsequently converted to surface coverage and reported as layers on the platinum surface. The coverage was determined by calibration with the C 1s XPS signal of the CO saturation coverage at 300 K[30]. At 300K, CO is known to saturate producing a uniform monolayer with coverage of 0.49 ± 0.02 (1 CO molecule for every 2 Pt atoms). Comparison of this saturation with the intensity dependence of the carbon signal from anisole allowed us to determine the saturation coverage of anisole and hence the coverage of every other dose. Dosage of anisole on Pt(111) shows a saturation plateau in the C1s area corresponding to 1 anisole molecule for every 10 Pt atoms (Supporting Information, Figure S1). We define this coverage as one monolayer (1 ML).

XPS

XPS spectra were recorded on a Specs GmbH system (XR50 X-ray source and Phoibos 100 SCD analyzer) using a standard Al Kα source (1486.7 eV) operated at 380 W

(14.6 kV, 26 mA). Selected peaks were obtained in high-resolution spectra using 0.05 eV step size, 1 second dwell time, and a pass energy of 30 eV. For the C1s and O1s regions 8 and 6 scans respectively were acquired to increase the signal to noise ratio. The spectra were then fit using CasaXPS analysis software using a mixed Gaussian-Lorentzian function and Shirley background subtractions for the C1s region while a linear background subtraction was used for the O1s region.

For the experiments, anisole was dosed on the clean sample at 115 K and then heated up to the desired temperature of observation to acquire the spectrum. Once the acquisition was done, the sample was subject to a cleaning cycle (Ar sputtering followed by annealing to 1100 K) to remove all the residual carbon on the surface. The cleanness of the sample surface was verified by LEED and XPS. This process was repeated for each dosage of interest.

TPD

The TPD experiments require placing of the sample in front of a differentially pumped quadrupole mass spectrometer (QMS) and ramping the sample temperature while monitoring the fragments of interest. For our experiments, the Pt(111) sample was dosed with varying exposures of anisole at 110 K and placed 1 mm below a 1 mm diameter hole leading to the differentially pumped QMS. The temperature controlled heating ramp was programmed in LabView and designed to provide and record a linear temperature ramp in the range of 120 K to 800 K, with a ramp rate of 7 K/s. The sample was subject to one cleaning cycle (Ar sputtering followed by annealing to 1100 K) to insure the cleanness of the surface before each dosage. A total of 11 channels corresponding to m/z values of 108, 94, 78, 77, 65, 45, 32, 28, 16, 15 and 2, were monitored for the anisole TPD experiments. The selected m/z values correspond to the main peaks of the fragmentation pattern of the expected species.

Computational Details

The DFT calculations were performed using the Vienna Ab Initio Simulation Package[31–33] (version 5.3) with the optPBE non local functional.[34,35] This functional was recently shown to correctly describe both chemisorption bonds and dispersive interactions and to give adsorption energies in close agreement with single-crystal calorimetry for unsaturated hydrocarbon molecules on Pt(111).[36,37] The electron-ion interactions were treated using the Projected Augmented Wave (PAW) method.[38] The plane wave basis set was truncated at a

cut-off energy of 400 eV. The geometric structures were considered as converged when the forces were less than 0.02 eV/Å.

When a metal surface was involved, a 4 layer p(4x4) slab model was considered, with 5 other equivalent layers of vacuum between slabs and the integration over the Brillouin zone was performed using a 3x3x1 Monkhorst-Pack k-points mesh.[39] For gas phase calculations, the energy was calculated at the gamma point in a cubic cell of 20×20×20 $Å^3$.

The local minima were located using the conjugated gradient method. The transition states were identified using the Nudged Elastic Band (NEB) method[40,41] and/or the dimer method.[42–44] To accurately locate the transition states, the structures were optimized using the Quasi-Newton method. For each optimized structure, a frequency calculation was finally performed to check its first order saddle point property.

All the frequency calculations were performed relaxing only the coordinates of the adsorbates and the upmost platinum layer. They were performed to calculate the ZPE correction as well as the vibrational entropy at 400 K within the harmonic oscillator approximation. For each structure involving a slab, the two softest modes of the bare slab were identified and removed for the evaluation of the entropy, keeping the number of vibrational modes constant from one structure to another. For gas phase hydrogen, both the rotational (free rigid rotator approximation) and the translational (free particle in a box model, pressure of 10^{-10} mbar *i.e.* roughly the pressure of the chamber) contributions were also calculated. For the other gas phase products (carbon monoxide, benzene and phenol), the free energy was not calculated since the partial pressures are very ill defined. Being mainly interested in barriers though, we associated to each desorption process a fictitious *desorbing transition state* meant to estimate the free energy barrier of desorption. The corresponding electronic energy and vibrational entropy were calculated from gas phase structures, and, to that, a 2D-translational entropy contribution (free particle on a 2D surface, the area of which equals the slab area) was added as earlier suggested by Campbell and co-workers.[45]

The XPS calculations were performed using the final state approximation, excitation of half a core electron to a virtual orbital. The excited electrons are allowed to relax after the core hole has been removed; all the remaining core hole electrons are frozen. Each atom was excited independently whatever its chemical nature. This method cannot provide absolute core level binding energies; only shifts of the core electron binding energy are relevant.[46,47]

Experimental Results.

XPS

The identification of surface species was initially performed by monitoring the carbon and oxygen environment of surface species as a function of temperature.

Figure 1 shows C1s photoelectron spectra after deposition of 8.1 L of anisole on Pt(111), acquired at varying temperatures. This dosage corresponds to an overly saturated layer, perhaps better described as the onset of overlayers of anisole on the surface (see Figure S1) and hence we refer to it as a multilayer regime. Upon deposition at 110 K, anisole shows two peaks in the C1s spectra, one at 285.3 eV, which is attributed to carbon bound to an oxygen atom (labeled C-O) and the other one at 283.7 eV, which is attributed to carbon atoms bound only to other carbons (labeled C-C).[28] After flashing to 240 K, the C-C and C-O areas decrease in intensity as some desorption takes place. At 360 K, the C-O peak area vanishes while the C-C peak area decreases only slightly in intensity. This is consistent with the decomposition and desorption of oxygen containing species. Upon heating to 550 K, the remaining C1s peak shifts to lower energy, 283.3 eV, as adventitious carbon accumulates during the time of the experiment.

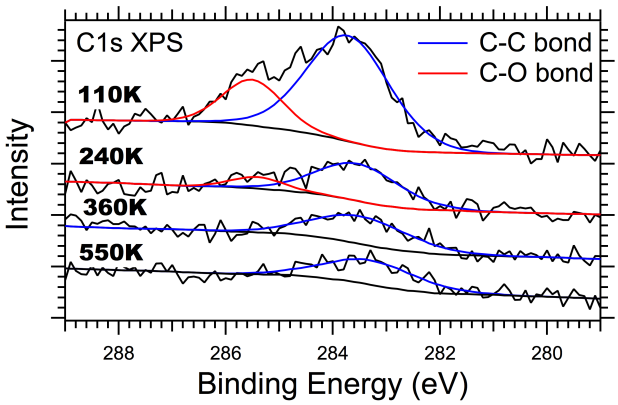

Figure 1. XPS spectra acquired at different temperatures starting from a multilayer of anisole deposited at 110 K

A closer look at the sub-monolayer regime is provided in *Figure 2* where the Pt – anisole interactions are dominant. Upon deposition of 0.5 ML of anisole on Pt(111), the spectrum at 115 K shows the two characteristic peaks (C-C and C-O) in the C1s region. The monolayer was determined as described in the experimental section and it is defined as one anisole molecule per 10 Pt surface atoms. Upon heating to 200 K and then 300 K, we notice no difference in the intensity of the peaks or in the electron binding energies. At 400 K, the C-O peak vanishes completely while the C-C peak intensity remains constant, and at the same binding energy of 283.5 eV. The extinction of the O1s XPS signal (Supporting Information, Figure S2) further corroborates the disappearance of the oxygen containing species.

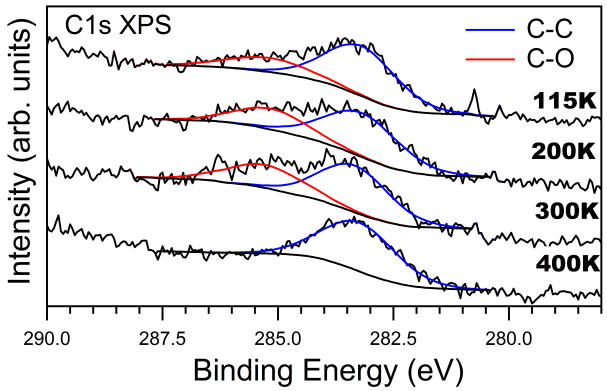

Figure 2. XPS C1s spectra acquired at different temperatures starting from 0.5 ML of anisole deposited at 115 K

Temperature Programmed Desorption

Molecular desorption of the parent anisole molecule was monitored for multiple values of coverage as a function of temperature (Figure 3, top panel). The data shows no molecular desorption of anisole at low coverages (0.6 ML and below). As we increase the coverage and reach 0.9 ML we notice that a part of anisole molecularly desorbs with a broad peak at ~400 K. This peak keeps shifting to low temperatures as we increase the coverage stabilizing at 360 K. For very high coverages a growing desorption peak at 260 K is observed and it corresponds to the multilayer desorption. This temperature appears to be higher than what was determined by XPS experiments (<240 K), however taking into account the XPS experimental time (~1h vs. seconds for TPD) and the residence time of species on the surface, the two experiments are consistent. For example, the desorption of anisole from a physisorbed layer has a half-life of 1.79×10^{-17} h at 115K so that the physisorbed layer can be considered as kinetically stable. When the temperature increases around 220-240 K, the half-life drops drastically to a fraction of an hour. Since the XPS experiment lasts one hour, the desorption actively occurs and this results in a change in the XPS spectrum at 240 K. This agreement holds for other species observed to desorb at higher temperatures where the apparent discrepancy is bigger but the residence time of species on the surface is lower (see Table S1 for the half-lives of different species as a function of temperature).

The primary desorbing product of anisole decomposition is benzene as observed by TPD (Figure 3, middle panel). No other aromatic species were observed. The TPD spectrum for the benzene fragment (mass 78) shows that, for all coverages below 1 ML, benzene molecularly desorbs from the surface in a broad feature from 360 K to 500 K. As we increase

the coverage above the monolayer the benzene desorption temperature centers to 400 K and we start seeing a growing peak at 260 K. Based on the measured fragmentation pattern of anisole in our QMS, this peak (marked with * in Figure 3) is not a reaction product, but rather due to the fragmentation of the molecularly desorbed anisole (see Supporting Information, Figure S3). The peak at 400 K does not seem to saturate, suggesting a different reactivity.

H_2 and CO are the only other observed reaction products (Figure 3, bottom panel). Hydrogen shows peaks at 325 K and 460 K, with two shoulders at 425 K and 510 K. For comparison, the associative desorption of pure hydrogen from Pt(111) has been previously observed in the temperature interval between 290 and 375 K.[48,49] The dot-dash line in Figure 3 that matches the observed peak in these experiments, corresponds to the reported dosage of 2 L of H_2 on clean Pt(111).[48] The additional high temperature hydrogen peaks have been assigned to subsequent surface reactions yielding H_2 as a product (see discussion below). Only one peak of CO is observable at 470 K. This desorbing molecular CO matches the temperature range of molecular desorption of CO from clean Pt(111) (dashed line on Figure 3).[50] The reactivity of anisole on Pt(111) surface is coverage dependent. The main goal of this study is to focus on the monolayer regime to correlate the experimental data to DFT calculations. The 0.9 ML, 1 ML and > 1ML exposures of anisole show the same behavior in the evolution of H_2 and CO.

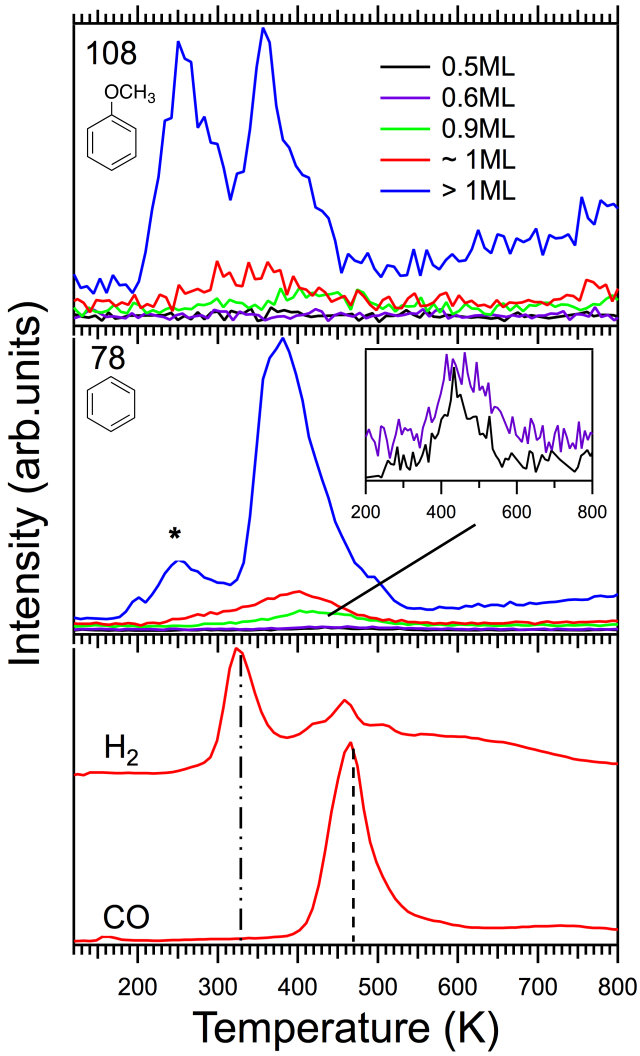

Figure 3 TPD spectra after anisole exposure on Pt(111) and selecting Anisole and formed byproducts (Benzene, Hydrogen and Carbon-monoxide). Different exposures of anisole have been dosed at 115 K on Pt(111) and desorption rates are measured using a linear temperature ramp of 7 K/s. (*) corresponds to benzene produced by the gas phase fragmentation pattern of anisole in the mass-spectrometer. The dashed line for CO corresponds to molecular desorption of pure CO from Pt(111) with 0.3 ML coverage.[51] *The dot-dashed line for H_2 corresponds to the expected desorption temperature of Hydrogen from Pt(111).*[49]

Analysis of the TPD data allows the experimental determination of desorption energies for each species (Table 1). The approach taken is based on the general rate law for desorption, the Polanyi-Wigner equation (eq. 1), where ν is the frequency factor and $\Delta_{des}E$ is the desorption activation energy for an nth order process.

$$-\frac{d\theta}{dt} = \nu\theta^{n} \exp\left(-\frac{\Delta_{des}E}{RT}\right) \qquad (1)$$

We use the simple approach of Redhead to obtain the general expression shown in equation 2. More complex and accurate methods exist for TPD analysis,[52] but the complexity of the chemical systems and the overlap of peaks make the Redhead method more suitable. Traditionally in the Redhead approach, the frequency factor ν takes the standard value of ~10^{13} s^{-1}. However Campbell *and co workers*[53–55] have demonstrated that a more accurate value can be calculated using the entropy of the adsorbed and gaseous species. The calculated frequency factors are presented in Table 1 as obtained using the Campbell approach for molecular or associative desorption and temperature corrected entropy values from the Yaw's Handbook.[56] With these appropriate frequency factors and using the TPD data, the desorption activation energy $\Delta_{des}E$ was calculated from the peak temperature T_p of each species of interest using (eq. 2).

$$\frac{\Delta_{des}E}{RT_p^2} = \frac{n\nu\theta^{n-1}}{dT/dt}\exp\left(-\frac{\Delta_{des}E}{RT}\right) \quad (2)$$

The TPD spectra also provide effective information of the activation energy associated with surface reactions. The high temperature peaks in the hydrogen TPD correspond to H_2 generated at a temperature above its normal desorption temperature and hence the associated activation energy calculated corresponds to the process that generates the additional H atoms. This quantity, calculated also using equation 2, is labeled as the apparent activation energy, $\Delta^{\ddagger}E_{app}$. It is important to note, however, that because hydrogen desorbs molecularly but is produced on the surface as an atomic species, desorption spectra can be analyzed as a first order molecular process or as a second order associative process. Both analyses are presented in Table 1 for comparison and the validity of the appropriate activation energies will be discussed in comparison with DFT computed values.

Table 1. Desorption energies of observed species, calculated by the Redhead analysis

Species	Observations	Temperature K	$\nu^{(a)}$ s^{-1}	$\Delta_{des}E$ kJ/mol	$\Delta^{\ddagger}E_{app}$ kJ/mol
Anisole	Multilayer	260	5.4×10^{16}	83	-------
	Saturated 1st ML	360	2.4×10^{17}	121	-------
	1st layer (low coverage)	400	4.2×10^{17}	136	-------
Benzene	Molecular desorption	400	4.3×10^{16}	125	-------

	Literature	400-550[57]	-------	133-200[57]	
Carbon monoxide	Molecular desorption	470	8.3×10^{14}	137	-------
	Literature	470[58]	-------	-------	-------
Hydrogen	Analyzed as molecular desorption	325	1.7×10^{14}		89
		425	1.8×10^{14}		118
		460	1.8×10^{14}		128
		510	1.8×10^{14}		142
	Analyzed as associative desorption	325	9.7×10^{8}	-------	52
		425	5.9×10^{8}	-------	67
		460	5.5×10^{8}	-------	73
		510	4.9×10^{8}	-------	81
	Literature	293-375[48]	-------	-------	39.7[48]
		330[49]	-------	-------	73[49]

[(a)] *Desorption frequency factors*

Analyzing the XPS and TPD results together allows us to determine the ratio of decomposition vs. desorption processes. In the XPS spectra at 240 K we can assume that the C-C peak corresponds to the monolayer coverage of anisole. At 550 K, all the anisole, benzene and CO has desorbed from the surface. Quantifying the remaining carbon left on the surface shows that 80% of the monolayer decomposes into carbon and only 20% desorbs from the surface. Taking a closer look to the TPD spectra of the saturated monolayer, mass 78 corresponds to the fragmentation pattern of anisole and benzene. Knowing the fragmentation ratio of anisole in the gas phase we can determine its contribution to mass 78. From the 20% desorption of the multilayer, 16% corresponds to the molecular desorption of benzene and 4% of anisole.

DFT Results

Anisole adsorption

We first studied the adsorption of anisole at different coverages and different geometries. The most stable structure of chemisorbed anisole was found at the so-called bri30 site, as earlier reported in the literature.[29,59,59–61] We computed the associated desorption energy on a p(4x4) slab and a p(3x3) slab in order to assess the coverage effect. On a p(4x4) slab (~0.6 ML with the definition given above), its desorption energy is 174 kJ/mol while on a p(3x3) slab (surface almost twice as covered, ~1.1 ML) it is about 140 kJ/mol showing a clear coverage dependence effect (see Figure 4). According to the experimental evaluation of saturation at one anisole for ten Pt, the p(3x3) slab models a close-to-saturation situation (one anisole for nine Pt).

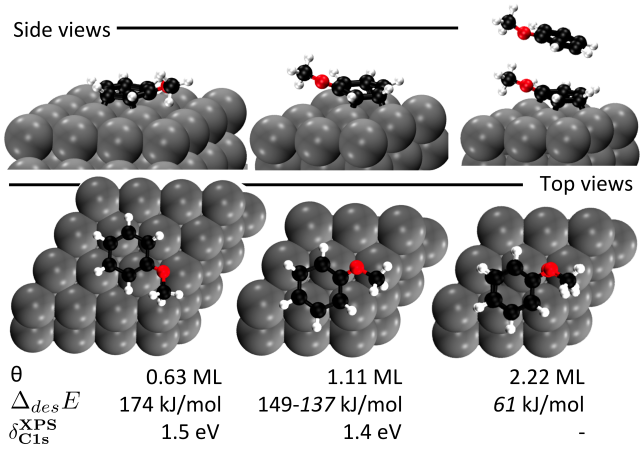

Figure 4: Structures of anisole at different coverages θ with their computed integral desorption energies $\Delta_{des}E$. One monolayer (ML) is defined as one molecule of anisole for ten surface platinum atoms. The energies in italics were computed with 14 layers of void between two slabs instead of 5. δ_{C1s}^{XPS} is the computed energy difference between the core level of carbon in the two environments, namely close to other carbons or close to an oxygen atom.

We went further and tried to model the situation corresponding to the bi-layer regime. We started from anisole on a p(3x3) slab and added another anisole molecule on top of the chemisorbed one with the same orientation of the methoxy MeO group (see Figure 4, right panel). In order to get rid of any non-physical interaction, we performed – only for this particular calculation – the geometry optimization with a larger void between the metallic slab and its periodic image, equivalent to 14 layers. The obtained structure and desorption energy (61 kJ/mol) must be compared with care to any experimental data. Static DFT is indeed usually not a method of choice to sample the phase space of such a flexible system. Nonetheless the potential energy surface should be rather flat since it is mainly based on weak van der Waals interactions. Therefore the energy should be quite reliable. Additionally, the carbon 1s electron binding energies were calculated for anisole on the p(3x3) and the p(4x4) slab and an XPS spectrum was simulated. The obtained separation δ_{C1s}^{XPS} between the C1s

signal for the C-C and C-O environments was 1.4 eV and 1.5 eV respectively, in good agreement with the measured separation of 1.6 eV.

Reactivity of the Methoxy substituent

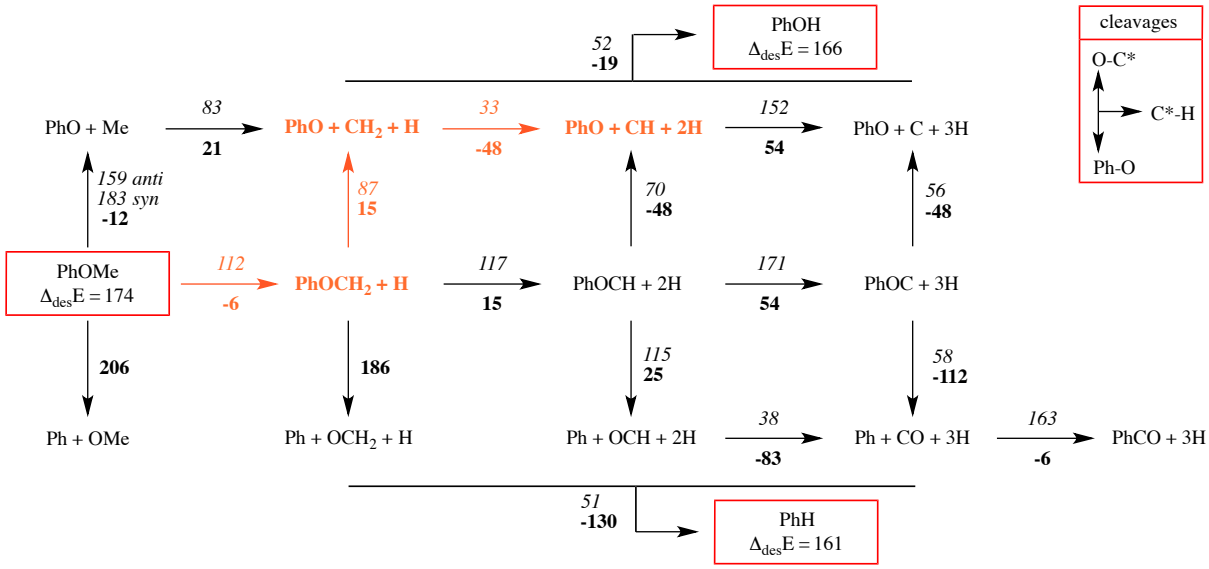

Figure 5. Sorted reaction network for the decomposition of anisole on Pt(111): rightward, upward and downward arrows show C-H, C*-O, Ph-O cleavages respectively. We assigned to each arrow the activation energy (in italics) and the reaction energy (in bold) of the elementary step. The reported energies are given in kJ/mol and are not ZPE-corrected. For the demethylation step,* anti *and* syn *precise the transition state of interest (see Figure 6, for the structures of the transition states).*

To investigate the anisole decomposition mechanism, we have first focused on the reactivity of the methoxy substituent, the carbon atom of which is referred to as C*. We therefore assumed that the phenyl moiety remains intact during the decomposition process. This fair assumption, considering that benzene derivatives are the main desorbing products experimentally, will be discussed later on in the present work. Despite the simplification resulting from this assumption, the decomposition mechanism still involves many bond cleavages: C-O scissions, namely Ph-O and C*-O, on the one hand, and C*-H scissions on the other hand. The resulting reaction network is therefore quite dense and shows many intermediates and transition states. To represent all the ensuing possibilities, we built the sorted reaction network given in Figure 5. This diagram gives the reaction and activation energies (except when the reaction is too endothermic) of each elementary step from anisole. For the sake of efficiency, the energies have not been ZPE-corrected since many intermediates have appeared to be chemically irrelevant. In spite of all, the raw data presented here invite interesting comments concerning the reactivity of anisole on Pt(111). In Figure 5, vertical arrows show C-O cleavages: should they point downwards, it is a Ph-O cleavage

process otherwise it is a C*-O cleavage. Rightward arrows are associated to C*-H cleavages. Moving to the right in the diagram therefore corresponds to an increase of the dehydrogenation level of C*. If we focus on the Ph-O cleavages (downward arrows), we notice that the reaction gets more and more favored thermodynamically when moving to the right of the diagram with reaction energies going from +206 kJ/mol (for the fully hydrogenated methoxy substituent) to -112 kJ/mol (for the fully dehydrogenated substituent). The Ph-O cleavage is particularly endothermic for anisole and phenoxymethylene $PhOCH_2$: this comes from the associated products, namely methoxy and formaldehyde, that adsorb through an oxygen atom to the not especially oxophilic Pt(111) surface. When the dehydrogenation level of the substituent increases (see Supporting Information, Figure S6, for the structures), the resulting products, namely formyl CHO and carbon monoxide CO, start strongly interacting with the Pt(111) surface through their carbon atom: the reaction energies drastically drop then. The activation energies follow the same trend: increasing the dehydrogenation level lowers the barriers. That was also reported in the literature for other oxygenates such as ethanol on Pt(111).[62,63]

The same trends can be observed for the C*-O cleavages (upward arrows) but these steps tend to be kinetically easier and thermodynamically more favored than the Ph-O cleavages (except when the strongly chemisorbed carbon monoxide is formed). This is related to the production of carboradical intermediates CH_x ($x = 1 - 3$) that are particularly stable on platinum. Even phenoxy on Pt(111) can be seen as a carboradical: it has already been reported in the literature[28] that it has an oxocyclohexadienyl structure and it corroborates with the infrared spectrum we computed (see Supporting Information, Figure S4). It also explains its particular stability on Pt(111). One C*-O cleavage elementary step shows up as an exception (upper left hand corner): the direct demethylation of anisole into phenoxy and methyl is particularly difficult. Albeit thermodynamically slightly downhill (-12 kJ/mol), the activation barrier is huge (183 kJ/mol) considering a syn-demethylation (Figure 6a). Nonetheless we were able to significantly lower this barrier (to 159 kJ/mol) when considering anti-demethylation with an S_N2-like mechanism involving a Walden inversion (Figure 6b). As far as we know, this is the first time such a transition state has been reported in the literature for surface platinum catalyzed reactions. Its stability might be addressed to its tighter geometry (bonds about 0.3 Å shorter) that makes the methyl group better interact with both the oxygen atom and the surface. Although that transition state is too high in energy to be of any relevance later in this work, it might play an important role on other metallic surfaces or with other substituents that might stabilize further more the planar transition state.

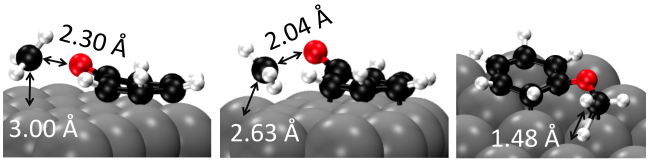

Figure 6. Selected transition states from anisole. (a) syn-demethylation ($\widehat{CPtO} = 86°$), (b) anti-demethylation with an SN2-like transition state structure ($\widehat{CPtO} = 123°$), and (c) first dehydrogenation of the methoxy MeO group.

PhO as a pivotal intermediate.

From the previous reactivity screening (Figure 5), we extracted the most favorable pathways yielding phenol and benzene and added the ZPE-corrections to build the corresponding free energy profiles at 0 K given in Figure 7.

As shown in Figure 7, the C*-O cleavage becomes the easiest process after the first dehydrogenation at C*. It leads to phenoxy PhO and methylene CH_2 on the surface, the latter evolving to methylidene CH, which is particularly stable on Pt(111). This agrees, at least qualitatively, with the experimental data of the group of Campbell[64,65] on the methyl-methylene-methylidene equilibrium. Phenoxy PhO is a pivotal intermediate. Its reactivity on the Pt(111) surface can yield either benzene or phenol. First, phenoxy can be very easily hydrogenated to phenol[19] (red path in Figure 7): the activation barrier is pretty low ($\Delta^{\ddagger}F = 27\ \mathrm{kJ/mol}$) and the reaction is thermodynamically favored ($\Delta_r F = -8\ \mathrm{kJ/mol}$). While phenol is easily formed on the surface, its desorption is rather difficult ($\Delta^{\ddagger}F = 164\ \mathrm{kJ/mol}$). An alternative consists in deoxygenating phenoxy into phenyl using methylidene CH (blue path in Figure 7) or atomic carbon C (green pathway in Figure 7). The key transition states towards the formation of phenyl are shown on Figure 8. The two overall barriers for benzene formation from phenoxy ($\Delta^{\ddagger}F = 144 - 153\ \mathrm{kJ/mol}$) are still higher than the one leading to adsorbed phenol, but slightly lower than that for the overall process including the phenol desorption ($\Delta^{\ddagger}F = 156\ \mathrm{kJ/mol}$). Although this 0 K study seems to support the selectivity for benzene over phenol, it is very delicate to compare barriers of a reaction at the surface and a desorption step since they involve quite different activation entropies resulting in rates that can be three orders of magnitude different.[53] A more detailed comparison therefore requires including the temperature and entropic contributions.

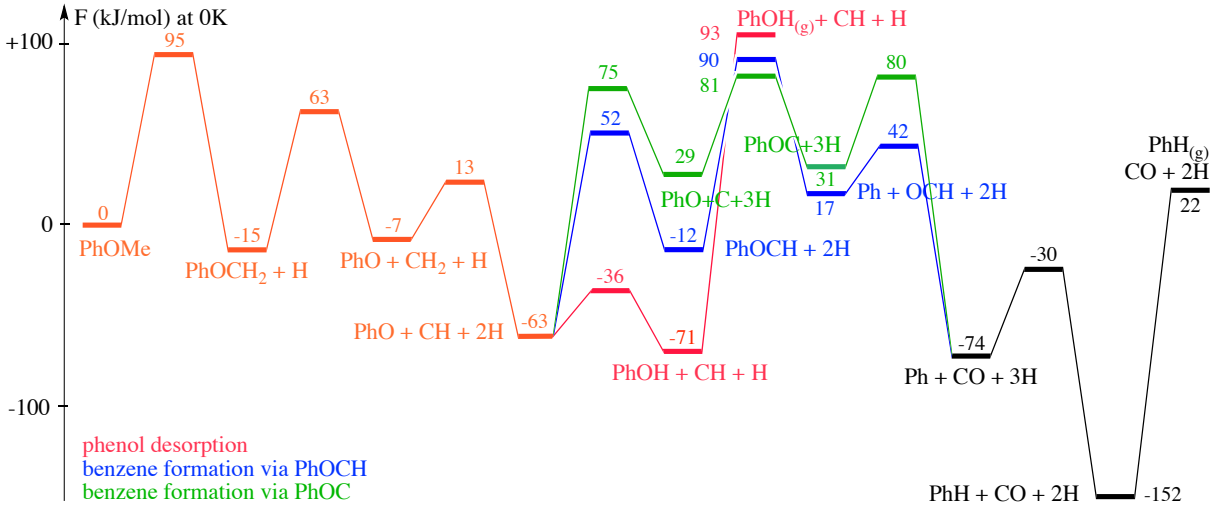

Figure 7. Energy profile (E+ZPE, in kJ/mol) on Pt(111) for the most favored anisole decomposition pathway forming the pivotal PhO (orange) followed by three possible pathways for its further transformation, namely phenol desorption, benzene formation via PhOCH (blue), and benzene formation via PhOC (green).

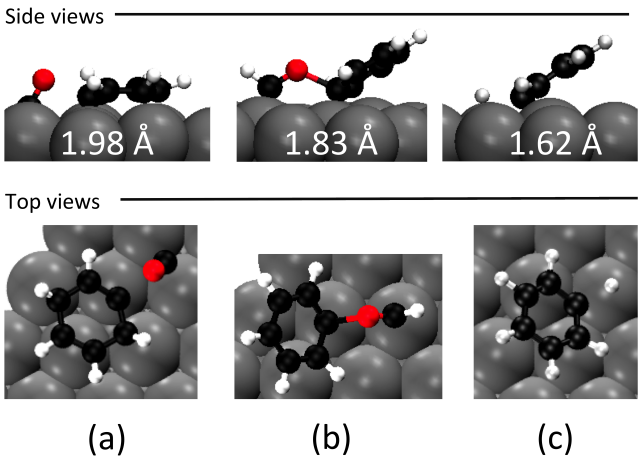

Figure 8. Transition states associated to phenyl formation from (a) PhOC and (b) PhOCH and (c) its hydrogenation to benzene. The distance of the bonds that undergoes cleavages are also given.

Entropic contributions

Modeling UHV conditions requires particularly special attention regarding the description of the desorption processes. Albeit endothermic, all the desorption processes become indeed extremely exergonic at higher enough temperature under these conditions. This is all the more important when trying to compare reactions with different amounts of gas phase molecules produced $\Delta_r n_g$:

$$PhOMe_{(g)} = PhOH_{(g)} + \tfrac{1}{2}\, H_{2(g)} + CH_{(ads)} \qquad \Delta_r n_g = +0.5 \qquad (3)$$

$$PhOMe_{(g)} = PhH_{(g)} + H_{2(g)} + CO_{(g)} \qquad \Delta_r n_g = +2 \qquad (4)$$

With the stronger increase in the number of gas molecules, benzene is clearly entropically favored, especially at low pressures. We assumed that the UHV chamber atmosphere mainly consists in hydrogen: its partial pressure is therefore well defined and we can calculate its desorption entropy. It is a key parameter since hydrogen is produced on the surface all along the three different pathways described in Figure 7. Albeit endothermic ($\Delta_{des}E = 89\,kJ/mol$), hydrogen desorption becomes exergonic – because of the entropic contribution ($\Delta_{des}S(H_2) = 433\,J.mol^{-1}.K^{-1}$) – for temperatures above 206 K. Below this temperature, the decomposition pathways should not change much. Above 206 K, we have to reconsider the steps that involve adsorbed hydrogen: each time hydrogen is produced, an extra exergonic step appears, namely hydrogen desorption, that stabilizes the system by 42 kJ/mol at 400 K. We end up with the free energy profile at 400 K given in

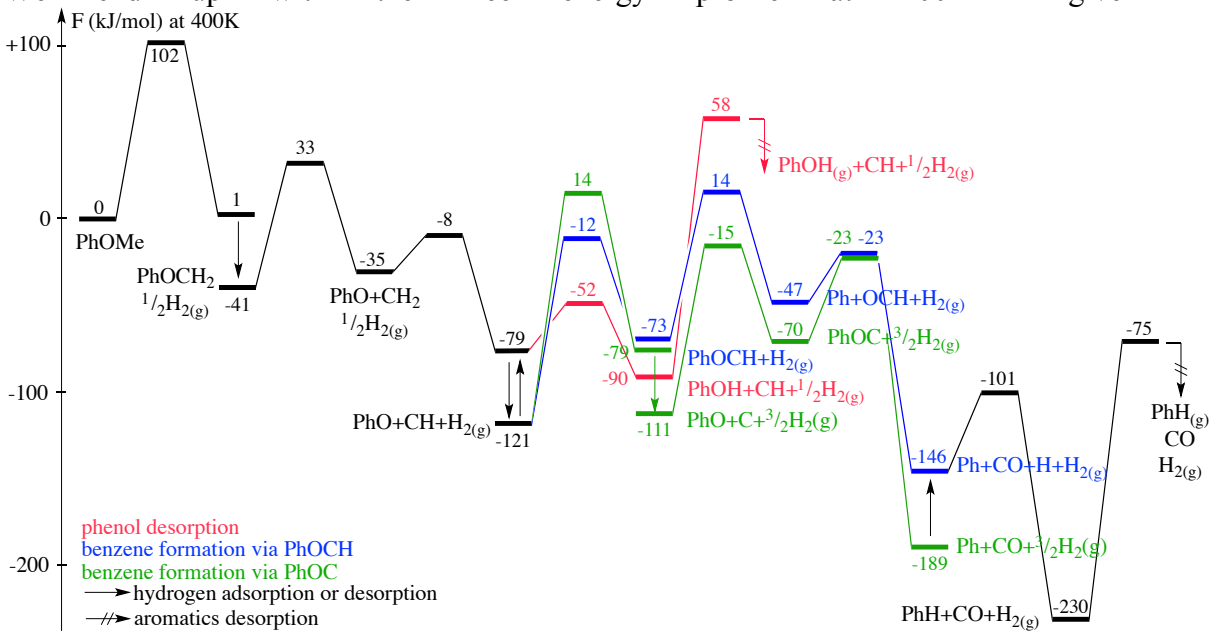

Figure 9.

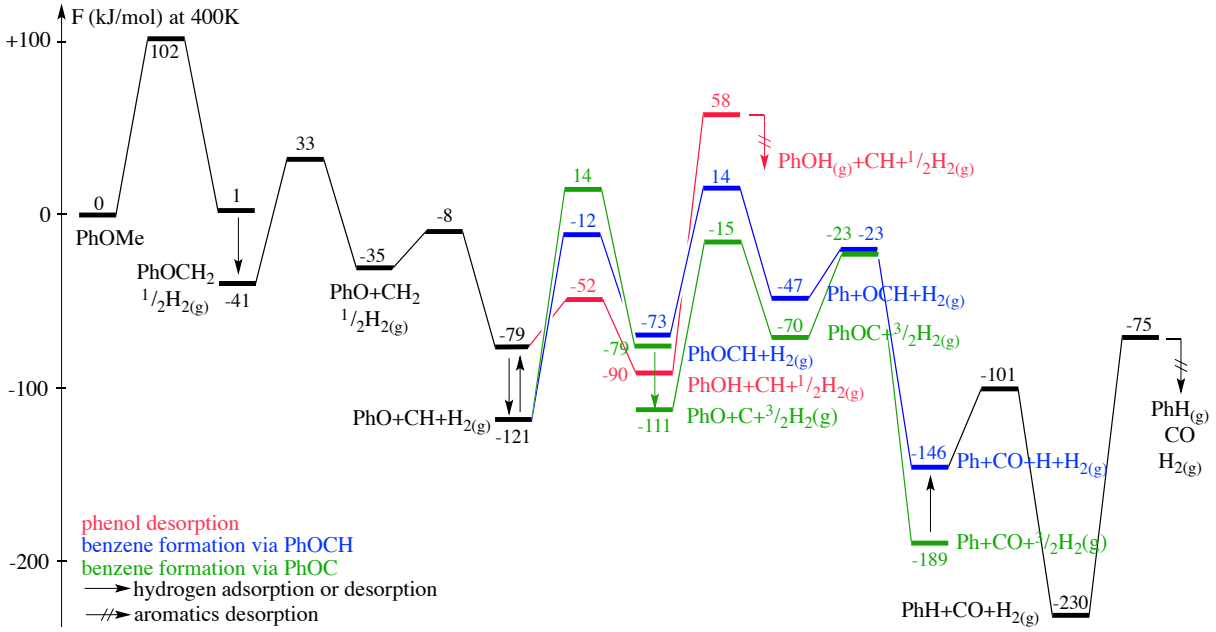

Figure 9. Free energy profiles at 400 K in kJ/mol using adsorbed anisole as a reference. Gas phase species are indicated with a (g) label. The barriers for phenol PhOH

and benzene PhH desorptions have been estimated with the desorbing transition state model described in the computational section.

As we can see in Figure 9, vibrational entropy slightly increases the barrier of the first dehydrogenation step from 95 kJ/mol to 102 kJ/mol. This results likely from the immobilization of the methoxy group with the proper conformation to perform the dehydrogenation with the optimal C-H-Pt alignment (see associated transition state given in Figure 6c). Then, with hydrogen desorption, the states {$PhOCH_2$+½$H_{2(g)}$} and {PhO+CH+$H_{2(g)}$} become highly stabilized: this is a consequence of Le Châtelier's principle. These hydrogen desorption processes do not drastically change the barrier involved in the production of benzene via PhOCH (blue path) since the rate determining transition state (Ph-OCH scission, lying at +14 kJ.mol^{-1}) does not involve any hydrogenation or dehydrogenation reactions. The production of benzene via PhOC (green path) is, on the other hand, more impacted by the hydrogen pressure. The dehydrogenation of methylidene CH to carbon C, which was energetically demanding ($\Delta_r E = +92\ \mathrm{kJ/mol}$), becomes more favorable ($\Delta_r F = +10\ \mathrm{kJ/mol}$) with the help of hydrogen desorption. With a rate determining transition state[66] lying at +14 kJ/mol, the green path becomes as easy as the blue path for the production of benzene. This can be directly related to the number of hydrogen released in the gas phase: 3/2 $H_{2(g)}$ in the case of the green path and 1 $H_{2(g)}$ for the blue path. With the release of only ½ $H_{2(g)}$, the production of phenol is clearly limited by the increase of the temperature: the desorption of phenol becomes much more difficult to reach ($\Delta^{\ddagger}F = 179\ kJ/mol$) from the rate determining intermediate {PhO+CH+$H_{2(g)}$}. The desorbing transition state associated to phenol desorption is admittedly stabilized by its 2D translational entropy but not as much as the intermediate {PhO+CH+$H_{2(g)}$}. Under TPD conditions, benzene formation is therefore easier than phenol production, with an overall effective activation barrier of 135 kJ/mol vs. 179 kJ/mol at 400 K, even though the conditions are much less reductive (low hydrogen pressure) than under catalytic conditions (large pressures of hydrogen).

Reactivity of the aromatic ring.

So far, we have assumed that the aromatic ring remains intact while the methoxy group of anisole undergoes several bond cleavages. As stable as the aromatic moieties might be, the drastic conditions of the UHV chamber favors all the dehydrogenation steps by generating gas phase hydrogen, as we have already mentioned in the previous part. In our attempt to understand the intrinsic reactivity of the most representative aromatic

intermediates, we have therefore screened the reactivity of several aromatic oxygenates, namely phenoxy, phenol, and anisole, toward C-H cleavages. The energetics (no ZPE-correction) of the first dehydrogenation step is given in Table 2. As a result of the adsorption of the aromatic ring at the bri30 site on Pt(111), no aromatic hydrogen atoms are equivalent. We labeled them with the usual *o*, *m*, and *p* tags (for *ortho*, *meta* and *para*) and we added the π/σ distinction (defined in Figure 10) to indicate whether the considered hydrogen is bound to a π or a σ bonded-to-Pt carbon atom. Strikingly, all the aromatic dehydrogenation reactions are endothermic and most of them involve huge barriers. The lowest barriers were computed for the *meta-σ* position, and, among the aromatic oxygenates studied, phenoxy shows the lowest energetic barrier ($\Delta^{\ddagger}\mathrm{E} = 128\ \mathrm{kJ/mol}$). This *meta* dehydrogenation was also reported by Ihm *et al.*[28] as being a key step in the aromatic ring decomposition of phenoxy. Along with another dehydrogenation in *ortho* (or *para*, but less likely scenario) they mention two C-C bond cleavages (*ipso-ortho* and *meta-para*) to form carbon monoxide CO and carbonaceous species on Pt(111). Using the same approach as in Figure 5, we studied the different C-C cleavages as a function of the hydrogen content of the aromatic ring (see Supplementary Information, Figure S5). Two routes have appeared to be chemically relevant: the first one consists of two *ipso-ortho* C-C cleavages followed by the aforementioned *meta*-dehydrogenation while the second one starts with the *meta*-dehydrogenation to afford an intermediate that decarbonylates with two subsequent *ipso-ortho* C-C cleavages (see Figure 11). At 0 K, the first mechanism shows a lower barrier ($\Delta^{\ddagger}\mathrm{F} = 162\ \mathrm{kJ/mol}$) than the second one ($\Delta^{\ddagger}\mathrm{F} = 186\ \mathrm{kJ/mol}$). Although the first mechanism should be preferred at lower temperatures, the barrier is far too big to be affordable. Increasing the temperature has almost no impact on the first mechanism ($\Delta^{\ddagger}\mathrm{F} = 159\ \mathrm{kJ/mol}$) but drastically changes the free energy landscape of the second one: the overall barrier of the latter strongly declines to $\Delta^{\ddagger}\mathrm{F} = 113\ \mathrm{kJ/mol}$. This second route, which was locked at lower temperatures, opens up with the help of hydrogen desorption. The associated rate-determining step switches to the meta-dehydrogenation at temperatures above 600 K. The full decomposition of phenoxy becomes therefore extremely efficient at higher temperatures.

Table 2. First aryl dehydrogenation energetics for adsorbed phenoxy PhO, phenol PhOH and anisole PhOMe. The reaction energies are given in bold and followed by the activation energy in italics. The energies are not ZPE-corrected.

$\mathbf{\Delta_r E}$, $\Delta^{\ddagger}E$ (kJ/mol)	*m*-π	*m*-σ	*o*-π	*o*-σ	*p*-π

PhO	**160**	**70**, *128*	**143**, *204*	**117**, *184*	**116,** *192*
PhOH	**155**	**68**, *150*	**157**, *208*	**82,** *174*	**116,** *163*
PhOMe	*not isolated*	**77**, *141*	**165**, *215*	**110,** *186*	**93,** *161*

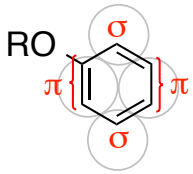

Figure 10. Labeling of the aromatic carbons for the flat-lying geometry of the organic species adsorbed at the bri30 site on Pt(111). Underlying Pt atoms shown as grey circles.

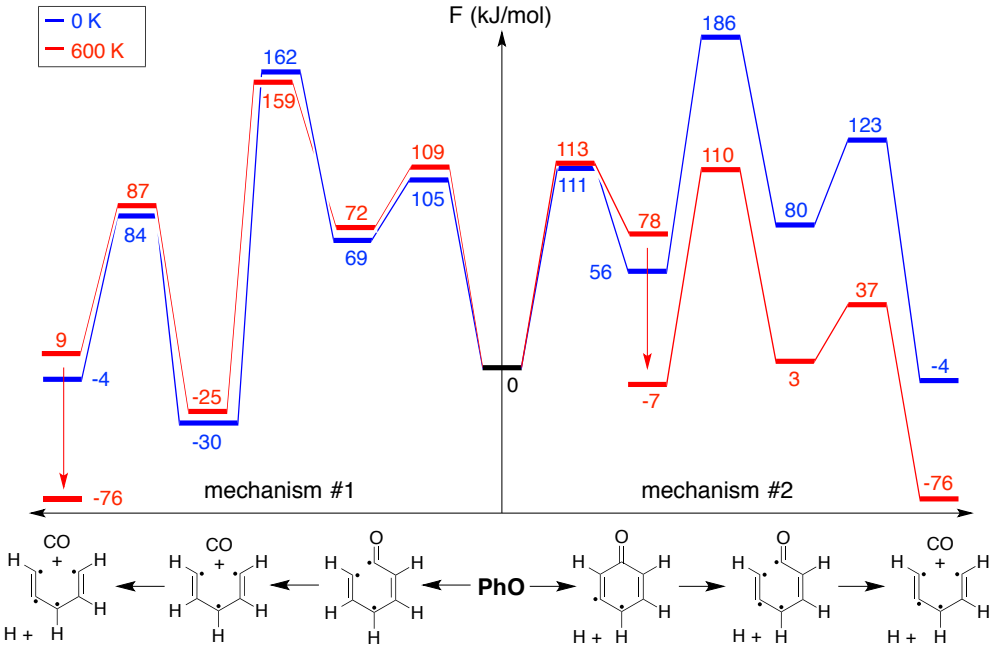

Figure 11. Decarbonylation of phenoxy into carbon monoxide and carbonaceous species.

Discussion

In our surface science experiments, anisole is deposited on a Pt(111) surface under Ultra High Vacuum (UHV) conditions at 110 K under higher and lower exposure conditions. Upon heating, four products desorb molecularly, namely anisole, hydrogen, benzene, and carbon monoxide. Interestingly enough, phenol has not been observed, while it is one of the main products in the hydrodeoxygenation reaction of aromatic oxygenates over the Pt/Al_2O_3 catalyst. Our approach, that combines results from TPD and XPS experiments on the one hand and DFT calculations on the other hand, allows us to address this selectivity for

benzene over phenol under TPD conditions. We propose the reaction scheme given in Figure 12. Under higher exposure conditions, the XPS spectra shows two C1s peaks one for carbon atoms bound to other carbon atoms and the other for carbon atoms bond to oxygen atoms. The concurrent intensity decrease of the two C1s peaks at 240 K, *ie*. at a rather low temperature, suggests that part of the anisole molecules are weakly bound to the surface and desorb easily. The TPD experiments estimate their desorption energy at 83 kJ/mol. This is in fair agreement with the DFT computed energy of 61 kJ/mol for a physisorbed layer on top of the flat-lying chemisorbed layer as shown in Figure 4. Those desorption energies are slightly higher than the vaporization enthalpy of anisole (which is about 40 kJ/mol[67]), as expected. Above 260 K, we end up with a mono or sub-monolayer chemisorbed system that is not necessarily equivalent to a submonolayer deposited directly. Evidence of the likely difference in the submonolayer regime can be found by the different ratio of reaction pathways. That is, upon initial adsorption of multilayers, the fraction of reaction leading to benzene products becomes dominant (see Figure 3).

Under lower exposure conditions (≤ 1 ML), the chemisorbed layer can keep desorbing molecularly. TPD experiments show indeed a molecular desorption peak at 360 K for a coverage about 1 ML and another one at 400 K at a coverage of 0.9 ML. This temperature shift reflects a variation of the experimental desorption energies from 121 kJ/mol to 131 kJ/mol that likely results from a decrease of the lateral interactions on a less crowded surface. DFT depicts well the desorption process with an energy of about 140 kJ/mol for a coverage of 1 ML that increases to 170 kJ/mol at 0.6 ML. No corresponding anisole desorption TPD signal could be observed at such a low coverage since desorption has become energetically too difficult to happen, and other reaction processes can take place.

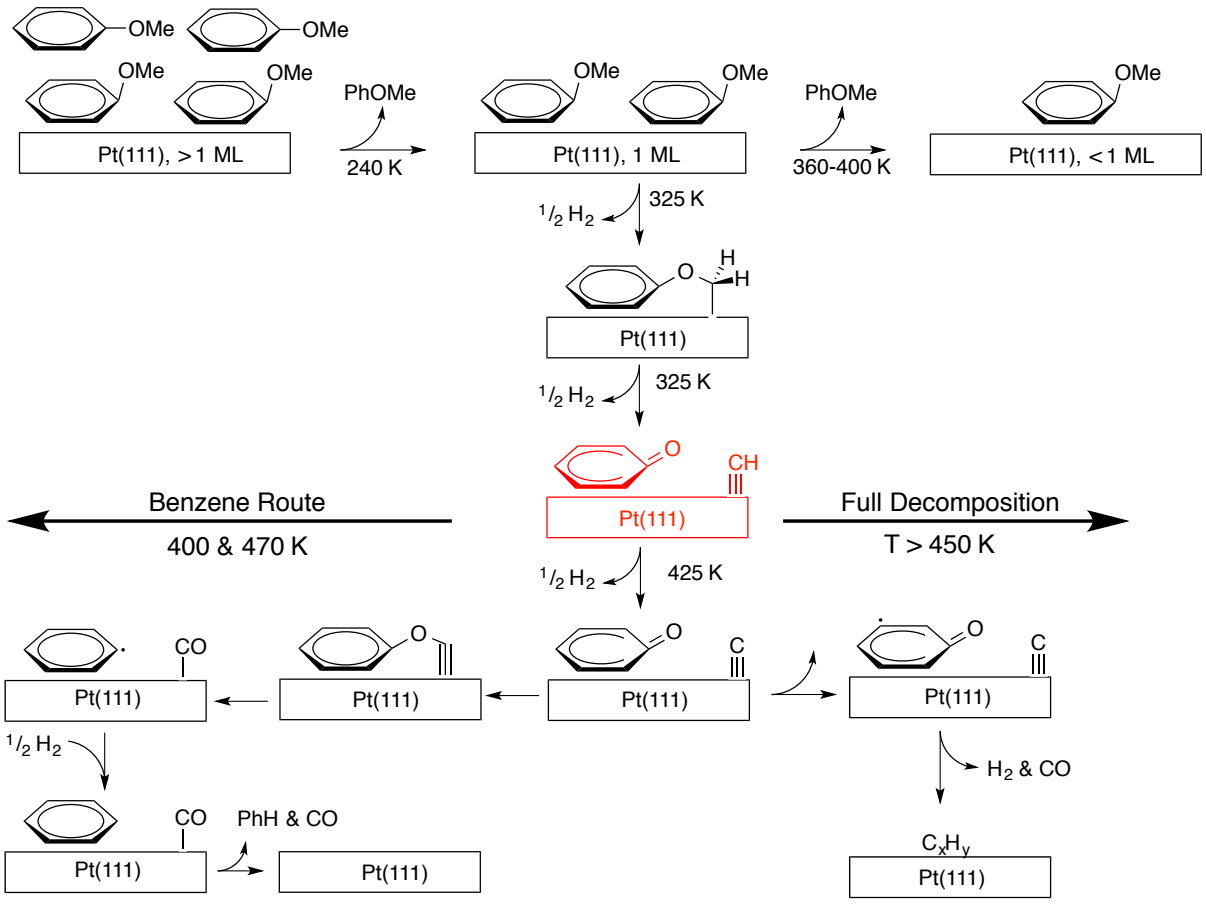

Figure 12. Proposed mechanism for anisole decomposition under UHV conditions on Pt(111) built form our DFT calculations and surface science experiments (the temperatures correspond to the TPD peaks).

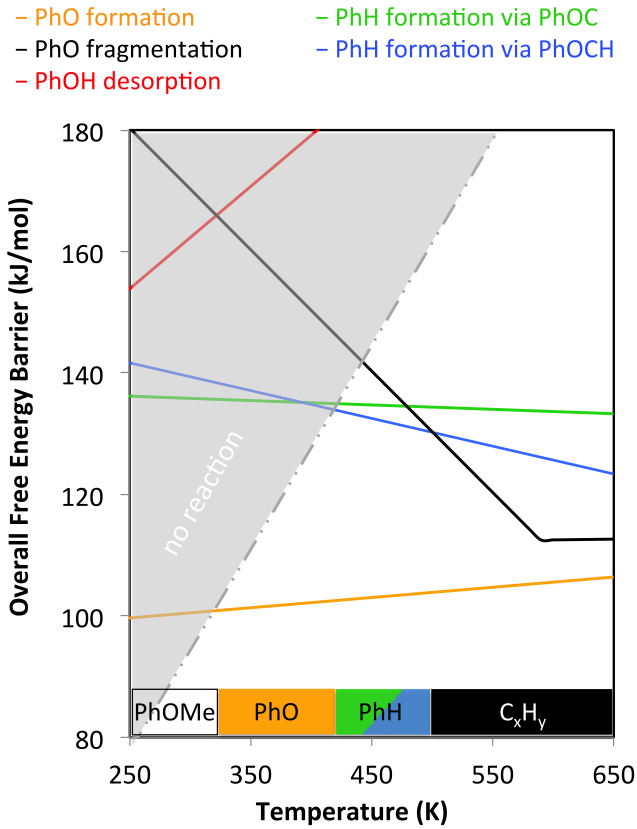

Figure 13. Free energy barriers as a function of temperature of the rate-determining steps associated to the four proposed mechanisms, after phenoxy formation (orange). The dotted curve splits the diagram in a kinetically forbidden and a kinetically allowed domain under the TPD conditions. The molar entropies were calculated at 400 K and assumed constant over the temperature range (Ellingham Approximation).

Our DFT investigation has lead us to consider many reactions. From the easy production of the pivotal phenoxy PhO intermediate, we have proposed two routes for benzene formation and one for phenol production. The competing fragmentation of phenoxy into carbonaceous species and carbon monoxide has also been described. Even if this whole inspection allows us to explain qualitatively the selectivity for benzene over phenol and the large amount of hydrogen released at higher temperatures, the comparison between DFT and TPD results remains, as things stand, out of range, since TPD gives temperatures and DFT free energies. To overcome this issue we plotted, see Figure 13, the overall barrier of free energy of each process as a function of temperature (solid curves). The dotted gray line splits the diagram into two domains: the upper gray half-space corresponds to kinetically difficult processes, and the lower white half-space shows kinetically crossable barriers (see Supporting Information for the mathematical development). With this new tool that we introduced, one can now give a detailed comparison between DFT and TPD to support the scheme given in Figure 12.

In Figure 13, the lowest barrier corresponds to the dehydrogenation of anisole PhOMe into {$PhOCH_2$+H} (orange line). This barrier is not much temperature-dependent and remains about 100 kJ/mol over the whole temperature range. Nonetheless, such a barrier is too high to be crossed at temperatures around 250 K, where anisole is predicted to be kinetically stable. When the temperature reaches 320 K, the orange curve crosses the kinetically forbidden gray domain to enter the kinetically allowed white half-space: the associated dehydrogenation of the methoxy substituent starts being effective. It is readily followed by a C*-O cleavage and another dehydrogenation process to yield phenoxy, methylidene and dihydrogen {$PhO+CH+H_{2(g)}$}, a state showing a particular stability ($\Delta_r F = -121$ kJ/mol at 400K). This is in excellent agreement with the TPD experiments that show one peak for hydrogen desorption at 325 K. This peak is particularly intense since it is associated to the desorption of two hydrogen atoms from anisole (over a total of 8 hydrogen atoms available). From the rate-determining intermediate state[66] {$PhO+CH+H_{2(g)}$} the overall free energy barriers to phenol (red curve), benzene (blue and green curves since two mechanisms have been studied), and coke formation (black curve) are also reported in Figure 13. The required adsorption of hydrogen (which is particularly endergonic under UHV conditions) for phenol production makes the phenolic route more and more difficult with the increase of temperature. This explains why no signal corresponding to phenol could have been detected in the TPD experiments.

Above 420 K, the overall barrier of benzene production via the rate-determining transition state {$PhO+[C\cdots H]^{\ddagger}+H_{2(g)}$} intersects the limit between the kinetically forbidden and kinetically allowed domains. We note that the other mechanism via the rate-determining transition state {$[Ph\cdots OCH]^{\ddagger}+H_{2(g)}$} is also possible from our DFT calculations. Nonetheless the shoulder at 425 K in the TPD of hydrogen seems to be consistent with the path through {$PhO+[C\cdots H]^{\ddagger}+H_{2(g)}$}. Therefore, hydrogen is produced from methylidene and further reaction steps readily follow and yield benzene. It agrees well with the TPD results that show a small hydrogen peak at 425 K and also a broad peak for benzene desorption at about 400 K (left path in Figure 13).

Above 450 K, the rate-determining transition state associated to the *ipso-ortho* C-C cleavage starts being reachable with the increased exergonicity resulting from the desorption of hydrogen and yield carbonaceous species (black curve in Figure 13). According to those DFT predictions, phenoxy can indeed undergo a dehydrogenation at the *meta* position, which seems to open up the route to the total decomposition of phenoxy into carbon monoxide, hydrogen, and carbonaceous species. This route becomes predominant over 500 K (lower

barrier than phenol and benzene productions). This is consistent with the TPD experiments that show the formation of hydrogen at 460 K and carbon monoxide at 470 K. This is supported by the XPS experiments that show the disappearing of the peak associated to carbon atoms bound to oxygen atoms: a C-O bond(s) containing species desorbs upon heating leaving hydrogenated carbonaceous fragments behind on the surface. The TPD of hydrogen is also to be compared with the one *Ihm et al.* [28] obtained when they studied the TPD of phenol on Pt(111). They show the same "peak-shoulder-band" pattern for hydrogen desorption over 460 K, which was attributed to the decomposition of phenoxy into $\{C_3H_3+CO+C_2+H_{2(g)}\}$ (460 K peak) and then $\{Cx+5/2H_{2(g)}+CO_{(g)}\}$ (600 K band). The shoulder was interpreted by *Ihm et al.*[28] as being the superposition of the peak at lower temperatures and the band at higher temperatures. It stands as an indirect evidence that phenoxy is indeed produced on the surface in our TPD experiments of anisole on Pt(111). They also estimated the overall barrier of this decomposition mechanism at 128 kJ/mol and attributed it to the rate-determining dehydrogenation of phenoxy at the *meta* position. Our DFT calculations suggest indeed that the barrier lies between 110 to 130 kJ/mol when the fragmentation of phenoxy becomes predominant. For temperature above 600 K, the rate-determining step is also predicted to be the *meta*-dehydrogenation (black curve in Figure 13).

All in all, the chemically relevant regime under TPD conditions is then between 420 and 490 K. At low temperatures, the productions of benzene and phenol compete, but the surface is not hot enough to have the aromatic compounds desorb. When the temperature increases, hydrogen desorption gets more and more exergonic. It therefore favors the dehydrogenation processes and disfavors the hydrogenation processes. That is why the production of phenol through phenoxy hydrogenation gets more and more difficult with the increase of temperature, whereas benzene production is almost not impacted by the temperature variations. Eventually large amounts of hydrogen can be produced upon coke formation: even if this route is particularly difficult energetically, it is entropically aided and becomes the predominant path above 500 K.

Although realistic catalytic conditions are far from the TPD conditions, this study points out the central role of phenoxy and methylidene, on the one hand, and hydrogen desorption, on the other hand, in hydrodeoxygenation reactions of aromatic oxygenates extracted from lignin.

The kinetically favored initial reaction is the dehydrogenation of the methyl group followed by the C*-O bond cleavage to yield phenoxy. In lieu of getting hydrogenated, it reacts with the carbonaceous species generated from the methyl group of anisole itself. The

actual reducing agents are hence adsorbed atomic carbon atoms or methylidene (depending on the considered mechanism) and not hydrogen. This "hook-back" mechanism, performed by atomic carbon atoms adsorbed on the surface, is especially favored since it leads to the particularly stable carbon monoxide adsorbate. This chemistry is to be compared to the oxygen removal from furfural on Pt(111) mediated with an atomic zinc co-adsorbate that stands as the actual reducing agent.[68]

Even though hydrogen might not be as crucial as expected to deoxygenate aromatic compounds, it still plays a key role. At a slightly higher temperature, the dehydrogenation of the adsorbates does not only affect the methyl group but also the aryl moieties. This results in the total decomposition of the organic compounds into coke. Under catalytic conditions, the hydrogen pressure (ranging from about one atmosphere to tens of bars) prevents this aryl decomposition. Nonetheless hydrogen desorption is much less favored and the selectivity of benzene over phenol is lost. Moreover a methane production pathway may also be possible under catalytic conditions, so that the reducing carbonaceous species get removed from the surface. All in all, phenolic derivatives indeed turn out to be the main products in hydrodeoxygenation performed over Pt/Al_2O_3 under catalytic conditions.[10,69]

Conclusion

In this article, we carefully studied the decomposition of anisole at a Pt(111) surface, a platform molecule in the transformation of lignin into valuable compounds. From surface science experiments (TPD and XPS), we showed that the anisole decomposition in ultra high vacuum experiments yields mainly benzene and not phenol, in contrast with the catalytic tests performed with supported Pt catalysts under a H_2 atmosphere.

To rationalize those observations, we performed an extensive analysis of the reaction mechanism based on DFT using the optPBE functional and a periodic slab model. We carefully assessed the adsorption of anisole at various coverages from 0.6 ML to the physisorbed second layer. Then, a kinetic analysis based on our DFT data shows an excellent agreement with the TPD spectra we obtained experimentally, validating the reaction mechanism we proposed here. The critical intermediate is phenoxy PhO co-adsorbed with methylidene CH. As far as we understand the system, the pressure of hydrogen tunes the selectivity of the subsequent branching reactions. Under UHV conditions, the hydrogenation reactions are all extremely difficult and phenol is therefore not produced. Carbonaceous species, which cannot be hydrogenated into methane for example, remain on the surface and efficiently perform the deoxygenation of phenoxy around 400 K. Above 450 K, phenoxy gets

even more dehydrogenated leading to the full decomposition of phenoxy into coke and carbon monoxide.

Based on this study, we can now propose a better design of hydrodeoxygenation catalysts. To prevent the formation of coke, a sufficient pressure of H_2 is required. However to facilitate the formation of benzene over phenol, we need to promote the Ph-O breaking with a reducing agent able to stabilize the liberated oxygen atom. Promoters such as atomic zinc adsorbed on the platinum surface have been successful in the deoxygenation of furfural and very recently anisole.[68,70] In addition to the stabilization of the oxygen atom, it weakens the C=O double bond: this might explain why it works with the deoxygenation of phenolics since phenoxy, the rate determining intermediate, has a strong C-O bond that structurally looks like a double bond.

Supporting Information

Coverage calibration with C1s XPS
Oxygen XPS
Correction of TPD signal due to fragmentation of species in the mass spectrometer
XPS vs. TPD consistency
DFT predicted infrared spectrum of phenoxy, PhO
Reaction network for phenoxy decomposition
Kinetic analysis of the DFT data
Intermediates and transition states of the routes to benzene and phenol
Intermediates and transition states of the routes to phenoxy fragmentation
Structures in XYZ format of all the adsorbates mentioned.

Author Information

Corresponding authors:
JBG email: Javier.giorgi@uottawa.ca
PS email: Philippe.sautet@ens-lyon.fr

Acknowledgements

The authors thank the LIA FUNCAT for funding. They are also grateful to the Centre Blaise Pascal (CBP) and the Pôle Scientifique de Modélisation Numérique (PSMN) – at the École Normale Supérieure de Lyon – for the computational resources and assistance. JBG thanks the Natural Sciences and Engineering Research Council of Canada for funding.

References

(1) Zakzeski, J.; Bruijnincx, P. C. A.; Jongerius, A. L.; Weckhuysen, B. M. *Chem. Rev.* **2010**, *110*, 3552–3599.

(2) Ragauskas, A. J.; Beckham, G. T.; Biddy, M. J.; Chandra, R.; Chen, F.; Davis, M. F.;

Davison, B. H.; Dixon, R. a; Gilna, P.; Keller, M.; Langan, P.; Naskar, A. K.; Saddler, J. N.; Tschaplinski, T. J.; Tuskan, G. a; Wyman, C. E. *Science (80-.).* **2014**, *344*, 1246843.

(3) Li, C.; Zhao, X.; Wang, A.; Huber, G. W.; Zhang, T. *Chem. Rev.* **2015**, *115*, 11559–11624.

(4) Laurent, E.; Delmon, B. *Ind. Eng. Chem. Res.* **1993**, *32*, 2516–2524.

(5) Laurent, E.; Delmon, B. *Appl. Catal. A Gen.* **1994**, *109*, 77–96.

(6) Romero, Y.; Richard, F.; Brunet, S. *Appl. Catal. B Environ.* **2010**, *98*, 213–223.

(7) Jongerius, A. L.; Jastrzebski, R.; Bruijnincx, P. C. A.; Weckhuysen, B. M. *J. Catal.* **2012**, *285*, 315–323.

(8) Wang, H.; Male, J.; Wang, Y. *ACS Catal.* **2013**, *3*, 1047–1070.

(9) Wildschut, J.; Mahfud, F. H.; Venderbosch, R. H.; Heeres, H. J. *Ind. Eng. Chem. Res.* **2009**, *48*, 10324–10334.

(10) Nimmanwudipong, T.; Runnebaum, R. C.; Block, D. E.; Gates, B. C. *Energy & Fuels* **2011**, *25*, 3417–3427.

(11) Runnebaum, R. C.; Nimmanwudipong, T.; Block, D. E.; Gates, B. C. *Catal. Letters* **2011**, *141*, 817–820.

(12) Zhu, X.; Lobban, L. L.; Mallinson, R. G.; Resasco, D. E. *J. Catal.* **2011**, *281*, 21–29.

(13) Gao, D.; Xiao, Y.; Varma, A. *Ind. Eng. Chem. Res.* **2015**, *54*, 10638–10644.

(14) Saidi, M.; Rahimpour, M. R.; Raeissi, S. *Energy & Fuels* **2015**, *29*, 3335–3344.

(15) Zhu, X.; Nie, L.; Lobban, L. L.; Mallinson, R. G.; Resasco, D. E. *Energy & Fuels* **2014**, *28*, 4104–4111.

(16) Foo, G. S.; Rogers, A. K.; Yung, M. M.; Sievers, C. *ACS Catal.* **2016**, *6*, 1292–1307.

(17) Pepper, J. M.; Fleming, R. W. *Can. J. Chem.* **1978**, *56*, 896–898.

(18) Pepper, J. M.; Lee, Y. W. *Can. J. Chem.* **1969**, *47*, 723–727.

(19) Honkela, M. L.; Björk, J.; Persson, M. *Phys. Chem. Chem. Phys.* **2012**, *14*, 5849–5854.

(20) Lee, K.; Gu, G. H.; Mullen, C. A.; Boateng, A. A.; Vlachos, D. G. *ChemSusChem* **2015**, *8*, 315–322.

(21) Gu, G. H.; Mullen, C. A.; Boateng, A. A.; Vlachos, D. G. *ACS Catal.* **2016**, *6*, 3047–3055.

(22) Lu, J.; Heyden, A. *J. Catal.* **2015**, *321*, 39–50.

(23) Chiu, C.; Genest, A.; Borgna, A.; Rösch, N. *Phys. Chem. Chem. Phys.* **2015**, *17*, 15324–15330.

(24) Chiu, C.; Genest, A.; Borgna, A.; Rösch, N. *ACS Catal.* **2014**, *4*, 4178–4188.

(25) Lu, J.; Behtash, S.; Mamun, O.; Heyden, A. *ACS Catal.* **2015**, *5*, 2423–2435.

(26) Xu, X.; Friend, C. M. *J. Phys. Chem.* **1989**, *93*, 8072–8080.

(27) Serafin, J. G.; Friend, C. M. *Surf. Sci.* **1989**, *209*, 163–175.

(28) Ihm, H.; White, J. M. *J. Phys. Chem. B* **2000**, *104*, 6202–6211.

(29) Tan, Y. P.; Khatua, S.; Jenkins, S. J.; Yu, J.-Q.; Spencer, J. B.; King, D. a. *Surf. Sci.* **2005**, *589*, 173–183.

(30) Norton, P. R.; Davies, J. A.; Jackman, T. E. *Surf. Sci.* **1982**, *122*, 593–600.

(31) Kresse, G.; Hafner, J. *Phys. Rev. B* **1993**, *47*, 558–561.

(32) Kresse, G.; Furthmüller, J. *Phys. Rev. B* **1996**, *54*, 11169–11186.

(33) Kresse, G.; Furthmüller, J. *Comput. Mater. Sci.* **1996**, *6*, 15–50.

(34) Dion, M.; Rydberg, H.; Schröder, E.; Langreth, D. C.; Lundqvist, B. I. *Phys. Rev. Lett.* **2004**, *92*, 246401.

(35) Klimeš, J.; Bowler, D. R.; Michaelides, A. *J. Phys. Condens. Matter* **2010**, *22*, 022201.

(36) Yildirim, H.; Greber, T.; Kara, A. *J. Phys. Chem. C* **2013**, *117*, 20572–20583.

(37) Gautier, S.; Steinmann, S. N.; Michel, C.; Fleurat-Lessard, P.; Sautet, P. *Phys. Chem. Chem. Phys.* **2015**, *17*, 28921–28930.

(38) Kresse, G.; Joubert, D. *Phys. Rev. B* **1999**, *59*, 1758–1775.

(39) Monkhorst, H. J.; Pack, J. D. *Phys. Rev. B* **1976**, *13*, 5188–5192.

(40) Henkelman, G.; Uberuaga, B. P.; Jónsson, H. *J. Chem. Phys.* **2000**, *113*, 9901.

(41) Sheppard, D.; Terrell, R.; Henkelman, G. *J. Chem. Phys.* **2008**, *128*, 134106.

(42) Henkelman, G.; Jónsson, H. *J. Chem. Phys.* **1999**, *111*, 7010.

(43) Heyden, A.; Bell, A. T.; Keil, F. J. *J. Chem. Phys.* **2005**, *123*, 224101.

(44) Kästner, J.; Sherwood, P. *J. Chem. Phys.* **2008**, *128*, 014106.

(45) Gottfried, J. M.; Vestergaard, E. K.; Bera, P.; Campbell, C. T. *J. Phys. Chem. B* **2006**, *110*, 17539–17545.

(46) Köhler, L.; Kresse, G. *Phys. Rev. B* **2004**, *70*, 165405.

(47) Jugnet, Y.; Loffreda, D.; Dupont, C.; Delbecq, F.; Ehret, E.; Cadete Santos Aires, F. J.; Mun, B. S.; Aksoy Akgul, F.; Liu, Z. *J. Phys. Chem. Lett.* **2012**, *3*, 3707–3714.

(48) Christmann, K.; Ertl, G.; Pignet, T. *Surf. Sci.* **1976**, *54*, 365–392.

(49) Lu, K. E.; Rye, R. R. *Surf. Sci.* **1974**, *45*, 677–695.

(50) Steininger, H.; Lehwald, S.; Ibach, H. *Surf. Sci.* **1982**, *123*, 264–282.

(51) Norton, P. R.; Goodale, J. W.; Selkirk, E. B. *Surf. Sci.* **1979**, *83*, 189–227.

(52) Nieskens, D. L. S.; van Bavel, A. P.; Niemantsverdriet, J. W. *Surf. Sci.* **2003**, *546*, 159–169.

(53) Campbell, C. T.; Árnadóttir, L.; J. R. V. Sellers. *Zeitschrift für Phys. Chemie* **2013**, *227*, 1435–1454.

(54) Campbell, C. T.; Sellers, J. R. V. *J. Am. Chem. Soc.* **2012**, *134*, 18109–18115.

(55) Campbell, C. T.; Sellers, J. R. V. *J. Am. Chem. Soc.* **2013**, *135*, 13998–13998.

(56) Chase, Jr., M. W.; Davies, C. A.; Downey, Jr., J. R.; Frurip, D. J.; McDonald, R. A.; Syverud, A. N. *NIST JANAF thermodynamical tables 1985*; National Institue of Standard and Technology, 1986.

(57) Ihm, H.; Ajo, H. M.; Gottfried, J. M.; Bera, P.; Campbell, C. T. *J. Phys. Chem. B* **2004**, *108*, 14627–14633.

(58) McEwen, J.-S.; Payne, S. H.; Kreuzer, H. J.; Kinne, M.; Denecke, R.; Steinrück, H.-P. *Surf. Sci.* **2003**, *545*, 47–69.

(59) Bonalumi, N.; Vargas, A.; Ferri, D.; Baiker, A. *J. Phys. Chem. B* **2006**, *110*, 9956–

9965.

(60) Réocreux, R.; Huynh, M.; Michel, C.; Sautet, P. *J. Phys. Chem. Lett.* **2016**, *7*, 2074–2079.

(61) Bonalumi, N.; Vargas, A.; Ferri, D.; Bürgi, T.; Mallat, T.; Baiker, A. *J. Am. Chem. Soc.* **2005**, *127*, 8467–8477.

(62) Liu, B.; Greeley, J. *J. Phys. Chem. C* **2011**, *115*, 19702–19709.

(63) Ferrin, P.; Simonetti, D.; Kandoi, S.; Kunkes, E.; Dumesic, J. a.; Nørskov, J. K.; Mavrikakis, M. *J. Am. Chem. Soc.* **2009**, *131*, 5809–5815.

(64) Karp, E. M.; Silbaugh, T. L.; Campbell, C. T. *J. Phys. Chem. C* **2013**, *117*, 6325–6336.

(65) Wolcott, C. A.; Green, I. X.; Silbaugh, T. L.; Xu, Y.; Campbell, C. T. *J. Phys. Chem. C* **2014**, *118*, 29310–29321.

(66) Kozuch, S.; Martin, J. M. L. *ChemPhysChem* **2011**, *12*, 1413–1418.

(67) Chickos, J. S.; Acree, W. E. *J. Phys. Chem. Ref. Data* **2003**, *32*, 519–878.

(68) Shi, D.; Vohs, J. M. *ACS Catal.* **2015**, *5*, 2177–2183.

(69) Saidi, M.; Rostami, P.; Rahimpour, H. R.; Roshanfekr Fallah, M. A.; Rahimpour, M. R.; Gates, B. C.; Raeissi, S. *Energy and Fuels* **2015**, *29*, 4990–4997.

(70) Shi, D.; Arroyo-Ramírez, L.; Vohs, J. M. *J. Catal.* **2016**, *340*, 219–226.